DOI: 10.1002/cnma.201500016

Supercapacitors

Diameter-Controlled Synthesis and Capacitive Performance of Mesoporous Dual-Layer MnO_2 Nanotubes

Yunpeng Huang,[a] Zhengyong Liang,[b] Yue-E Miao,[a] and Tianxi Liu*[a]

Abstract: Mesoporous dual-layer MnO_2 nanotubes assembled from well-aligned MnO_2 nanosheets are synthesized via a facile and efficient sacrificial template method. To begin with, the self-standing carbon nanofibrous membranes are prepared via electrospinning and high-temperature carbonization, followed by an in situ redox reaction in $KMnO_4$ solution to coat the carbon nanofiber (CNF) template with MnO_2 nanosheets until the CNFs are consumed. The synthesized dual-layer MnO_2 nanotubes are composed of an inner shell of packed MnO_2, and an outer shell of mesoporous sheet-like MnO_2. Importantly, the dimensions of the MnO_2 nanotubes can be easily controlled by tuning parameters including CNF diameter and redox reaction temperature. The MnO_2 nanotube electrode thus prepared manifests excellent cycling stability with a specific capacitance of 231 $F g^{-1}$ and an areal capacitance of 309 $mF cm^{-2}$ for supercapacitors. This approach opens up a new way for designing MnO_2 nanostructures as promising electrode materials.

Introduction

Over the past decades, functional inorganic materials have attracted considerable interest for their wide applications including catalysts,[1–3] sensors,[4,5] optoelectronic materials,[6] energy storage,[7–10] etc. Among them, nanomaterials, especially one dimensional (1D) nanostructures, such as nanowires,[11,12] nanorods,[13] nanotubes,[14,15] nanofibers,[16] are studied intensively due to their peculiar and fascinating properties with respect to their bulk counterparts. Due to their interesting architectures and relatively high specific surface area, 1D nanotubes or hollow fibers have recently been extensively investigated and found to have wide applications in the fields of electrochemical sensors,[17] photocatalysts,[18,19] Li-ion batteries,[20–22] and supercapacitors.[23,24] Since the first discovery of carbon nanotubes (CNTs),[25,26] many methods including self-assembly,[27] chemical vapor deposition,[25] hydrothermal reaction,[28] template-directed synthesis[19,29,30] and coaxial electrospinning[17] have been reported for the synthesis of 1D nanotubes. However, most of the reported methods for synthesizing nanotubes are either tedious or expensive; they employ high-temperature processes, high-cost templates, and corrosive chemical treatments. Therefore, a versatile and straightforward method for preparation of 1D nanotubes is urgently needed.

As an important member of the transition metal oxides, MnO_2 shows great advantages compared with other members (e.g., Co_3O_4, Fe_3O_4, NiO, V_2O_5), such as low cost, environmental friendliness, natural abundance, and excellent electrochemical properties, and thus is widely applied in molecular/ion sieves,[31] catalysts,[32] and energy-storage applications.[33,34] It has been reported that the properties of nanomaterials depend not only on their chemical compositions, but also on their morphologies, dimensions, and size distributions.[35] Hence, various morphologies of MnO_2 have been developed in different forms, such as wires,[36] rods,[37] belts,[38] and tubes.[15] Liu et al. reported the synthesis of hierarchical hollow MnO_2 microspheres through a facile chemical method followed by selective HCl etching.[29] Lu and co-workers prepared highly ordered MnO_2 nanotubes and nanowire arrays via an electrochemical deposition technique using porous alumina templates.[15] Ma's group prepared a sea-urchin-shaped MnO_2 and a three dimensional (3D) hierarchical clew-like MnO_2 nanostructure through a template-free hydrothermal reaction.[39] Despite these achievements, rational preparation of 1D MnO_2 nanotubes still remains a challenge and is highly desirable.

Electrospinning is a simple and efficient method for fabrication of nanofibers with diameters in the range of nanometers to a few microns,[40,41] it provides a quite straightforward method for preparing a free-standing and mesoporous CNF matrix by post-carbonization of electrospun polymeric nanofibers.[42] In our previous study,[43] a facile sol-gel electrospinning method was used for the preparation of mesoporous SnO_2 nanotubes, and the subsequently engineered MoS_2/SnO_2 heterostructures exhibited excellent electrochemical catalytic performance. In this work, electrospun CNFs were used as a sacrifi-

[a] Y. P. Huang, Y.-E. Miao, Prof. T. X. Liu
State Key Laboratory of Molecular Engineering of Polymers
Department of Macromolecular Science
Fudan University
Shanghai, 200433 (P.R. China)
E-mail: txliu@fudan.edu.cn

[b] Z. Y. Liang
School of Chemical Engineering and Energy
Zhengzhou University
Zhengzhou, 450001 (P.R. China)

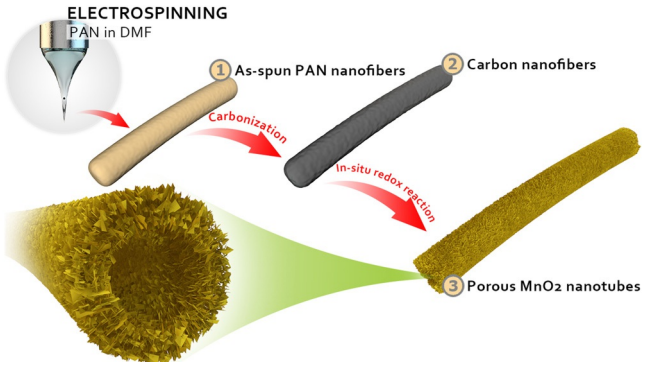

Scheme 1. Schematic illustration of the preparation of mesoporous MnO_2 nanotubes.

cial template for the preparation of MnO_2 nanotubes via a simple in situ redox reaction under mild conditions (Scheme 1). The as-synthesized MnO_2 nanotubes with a cavity diameter of about 200 nm were composed of an inner-shell of compact MnO_2 and an outer-shell of mesoporous sheet-like MnO_2. Parameters influencing the morphology of MnO_2 tubes, including CNF fiber diameters and reaction temperatures, were investigated and discussed. Finally, the as-prepared MnO_2 nanotubes were used as electrode materials for supercapacitors and showed good capacitive behavior. As far as we know, this is the first report regarding the fast and mass preparation of MnO_2 nanotubes using electrospun CNFs as a sacrificial template.

Results and Discussion

Morphological and structural characterization

PAN is the most widely utilized precursor polymer for commercial carbon fiber manufacturing. The heat treatment of PAN fibrils involves two processes of pre-oxidation and carbonization.[44] During the pre-oxidation in air at 250–300 °C, PAN fibrils undergo partial dehydrogenation and cyclization which make them compact and more stable to endure subsequent high-temperature carbonization and keep their fibrous structure. During the carbonization process, polymers begin to pyrolyze and a considerable amount of volatile by-products are released, and thus flexible and strong CNFs can be obtained.

Many factors can influence the electrospinning process and the morphology of the final products, especially solution properties such as polymer molecular weight, concentration, conductivity and surface tension.[41] In this work, the amount of PAN in the precursor solution was adjusted to prepare nanofibers with different diameters. As shown in Figure 1, the PAN6 fibers are ultrathin with a mean diameter of 120 nm (Figure 1 A). Upon increasing the PAN content within the precursor solution, the fibers become thicker with mean diameters of 230 and 770 nm for PAN10 (Figure 1 B) and PAN15, respectively (Figure 1 C). It is also notable that fibers are uniformly distributed in a random manner for all the samples. After subsequent carbonization, the fibers retain good morphology but slightly shrink due to the decomposition of PAN (Figure 1 D, 1 E, and 1 F).

The synthesis of MnO_2 nanotubes is performed using a simple in situ redox reaction in aqueous solution with an excess of $KMnO_4$. Because the growth of MnO_2 on CNFs is based on the substitution of carbon, complete reaction between CNFs and $KMnO_4$ will gradually consume the carbon until the CNF backbone is exhausted, thus the self-standing MNT film could be produced simultaneously. As shown in Figure 2 A–2 C, the diameter of the MNTs increases as that of the CNFs increases. The mean diameters for MNT6, MNT10, and MNT15 are 237, 683, and 1068 nm, respectively. The significant increase in diameters for MNTs with respect to their CNF counterparts is probably due to the formation of sheet- or whisker-like MnO_2 nanostructures, where the compact carbon is replaced by a mesoporous MnO_2 shell, thus leading to larger MNT diameters. It is also worth noting that the sizes of MnO_2 subunits in MNT6 are small but still larger than those in MNT15, while MNT10 subunits are the largest among them by

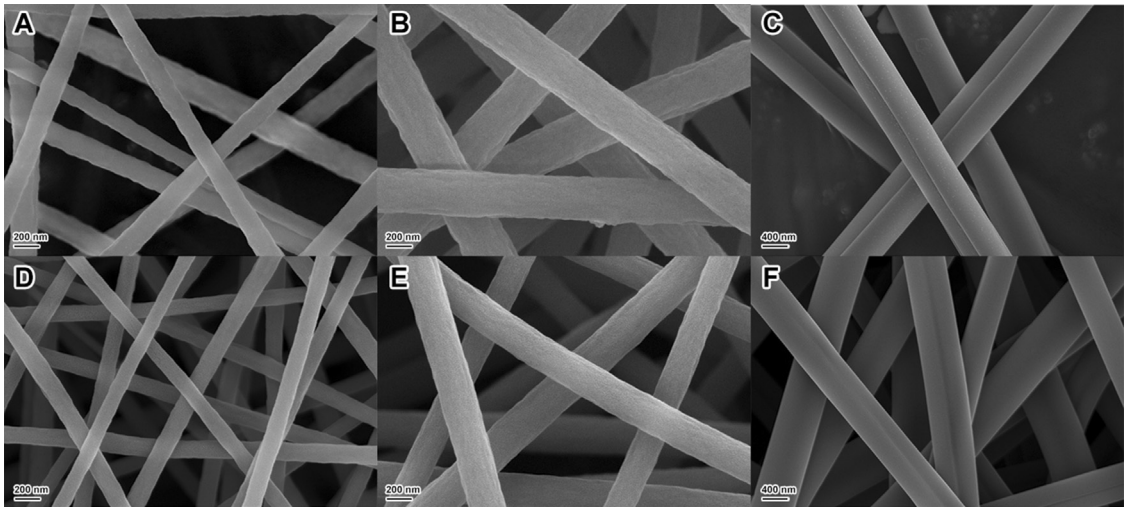

Figure 1. FESEM images of (A) PAN6, (B) PAN10, (C) PAN15 and (D) CNF6, (E) CNF10, (F) CNF15.

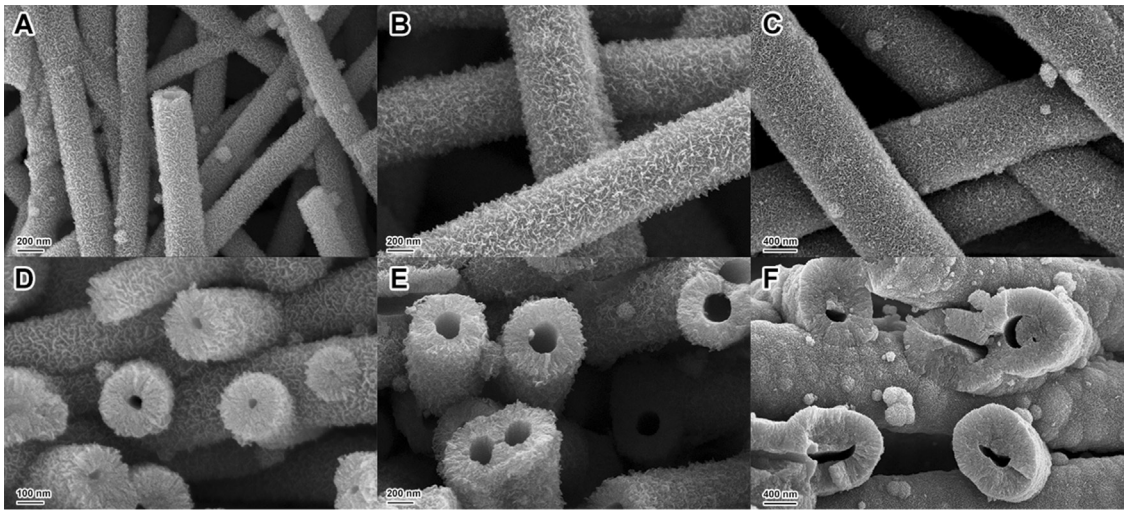

Figure 2. FESEM images of (A, D) MNT6, (B, E) MNT10 and (C, F) MNT15.

forming a more homogeneous distribution and better mesoporous structure. The formation of dense and closely packed subunits of MNT15 is probably because the thicker CNFs need more MnO_2 to substitute the carbon, thus leading to the packing of MnO_2 on the outer surface. Cross-sectional images of the MNTs reveal more details of the hollow structure of MnO_2. As can be seen in Figure 2D–2E, all MNTs hold cavities throughout individual nanofibers along the longitudinal axis, and both MNT6 and MNT10 have regular circular cavities. As for MNT15, the collapsed cavities result from the densely packed MnO_2, in which the interlayers are too weak to support the overweight outer layer. Notably, the cavity diameter for MNT10 is much larger than that of MNT6, which is derived from the diameter difference of the CNF templates.

To further investigate the influence of temperature on the morphology of MnO_2 nanotubes, MNTs were also prepared at various temperatures. As presented in Figure 3, MNT-40 has the smallest MnO_2 subunits and densely packed shell (Figure 3A and 3D), while the outer layer of MNT-60 is quite porous with sheet-like subunits (Figure 3B and 3E), and the case of MNT-90 is in between (Figure 3C and 3F). The mechanism for the differences can be explained as follows: at relatively lower temperatures (e.g., 40 °C), the reaction between carbon and $KMnO_4$ is quite slow, which is not desirable to form mesopores but favorable for the accumulation of products. When the reaction temperature is very high (e.g., 90 °C), $KMnO_4$ is prone to decompose to MnO_2 ($2KMnO_4 = K_2MnO_4 + MnO_2 + O_2$) rather than reacting with carbon, which will also cause the accumulation and packing. Therefore, mild reaction conditions of 60 °C are beneficial for the formation of mesoporous MnO_2 nanotubes.

From the TEM images presented in Figure 4, a well-defined hollow or tubular structure can be clearly observed in MNT10 (Figure 4A, denoted by red arrows) with a diameter of 680 nm. The porous MnO_2 shell is composed of an inner shell of closely packed MnO_2 with a thickness of about 114 nm, and an outer

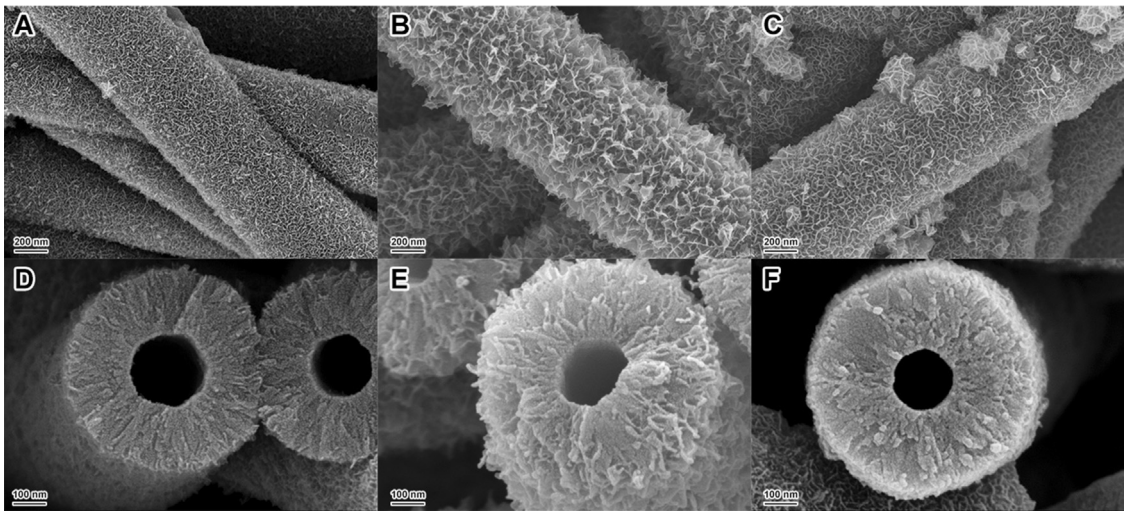

Figure 3. FESEM images of (A, D) MNT-40, (B, E) MNT-60 and (C, F) MNT-90.

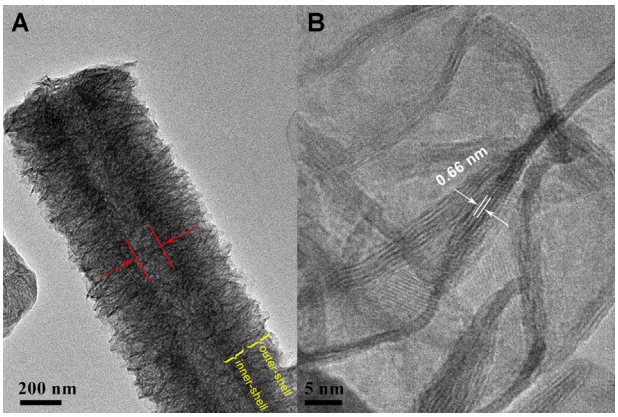

Figure 4. TEM and HRTEM images of MNT10.

shell of mesoporous sheet-like MnO_2 with a thickness of about 147 nm. This unique dual-layer structure can be attributed to a fast redox reaction rate at high $KMnO_4$ concentration, thus leading to the closely packed inner shell, while a slow reaction rate at a low $KMnO_4$ concentration will result in mesoporous sheet-like outer-shell structures. The HRTEM image in Figure 4B reveals an interplanar spacing of 0.66 nm for the MnO_2 nanosheets, corresponding to the (001) plane of birnessite-type MnO_2.[45] The crystal structures of MnO_2 nanotubes were examined by XRD (Figure 5A), in which the wide peak of CNFs at $2\theta = 25^\circ$ is associated with the amorphous structure of carbon. The diffraction peaks of MNT10 for $2\theta = 12^\circ$ and 37° can be readily indexed to the (001) and (021) crystal planes of birnessite type MnO_2 (JCPDS card No.18-0802). In the XPS spectra shown in Figure 5B, two peaks centered at 642.8 and 653.0 eV in Mn 2p spectrum can be assigned to the binding energy of Mn $2p_{3/2}$ and Mn $2p_{1/2}$, respectively, further confirming the dominance of MnO_2 in the product.

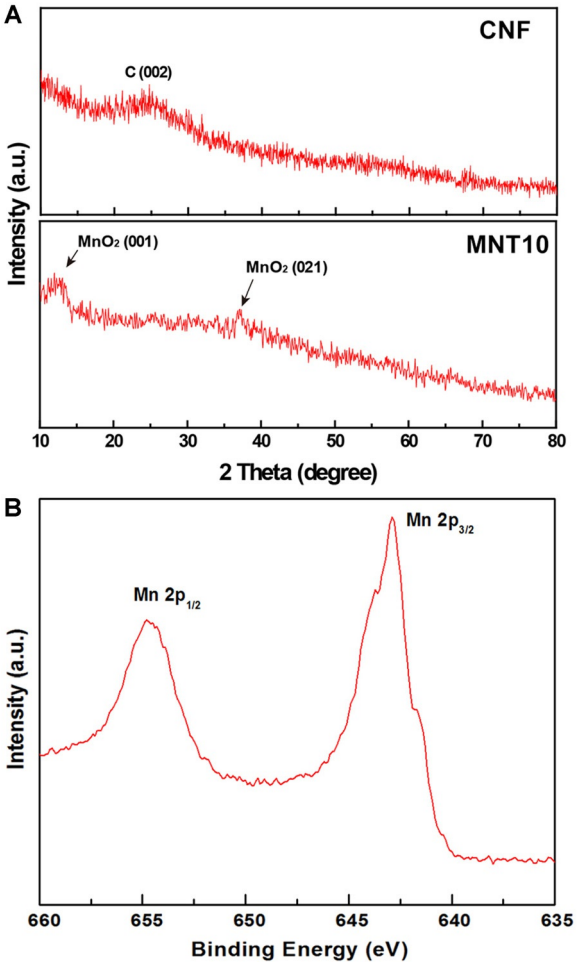

Figure 5. (A) XRD patterns of CNFs and MNT10, and (B) XPS spectrum of MNT10.

Electrochemical properties

Electrochemical measurements were performed with a standard three-electrode system in 0.5 M Na_2SO_4 solution to evaluate the electrochemical performance of mesoporous MnO_2 nanotubes. CV curves at a scan rate of 100 mV s^{-1} were used to investigate the electrochemical charge storage capacity of the MNT6, MNT10, and MNT15 electrodes, as shown in Figure 6A. All CV curves deviated from the ideal symmetrical rectangular shapes with a pair of weak redox peaks, indicating a typical pseudocapacitor characteristic. In particular, the MNT10 electrode has the highest specific current intensity with a moderately distorted rectangular shape, revealing that MNT10 has the best electrochemical performance. The specific capacitance of the MNTs was calculated from CV curves with Equation (1):

$$C = \frac{\int id\Delta u}{v\Delta um} \quad (1)$$

where i is the current (A) as a function of voltage, Δu is the voltage window (V), v is scan rate (mV s^{-1}), and m is the mass of electrode materials. The results are shown in Figure 6B, and areal capacitances of 281, 309, and 166 mF cm^{-2} and specific capacitances of 211, 231, and 125 F g^{-1} are respectively achieved for MNT6, MNT10 and MNT15, which are comparable or even superior to the results reported previously.[29,37,39] The better capacitive performance for MNT10 is ascribed to the porous MnO_2 outer shell and smaller wall thickness, which can facilitate electron transportation and ion diffusion.

Figure 7A shows the CV curves of MNT10 electrode at different scan rates in 0.5 M Na_2SO_4 aqueous solution. These curves are diamond-shaped with a pair of weak redox peaks, indicating good pseudocapacitive property and fast charging/discharging characteristic. The variation in the specific capacitance of MNT10 as a function of the scan rate is plotted in Figure 7B. At a high scan rate of 100 mV s^{-1}, the capacitance only retains 49 and 37 F g^{-1}, revealing the inferior rate capability of MNT10, which may be mainly due to its lower electrical conductivity. Figure 7C shows the constant current charge/discharge curves of the MNT10 composite at different current densities. It is clear that the charging curves are nearly symmetric with their corresponding discharging counterparts, with the plateau of the charging curve reflecting the pseudocapacitive nature of MnO_2 under a high current density of

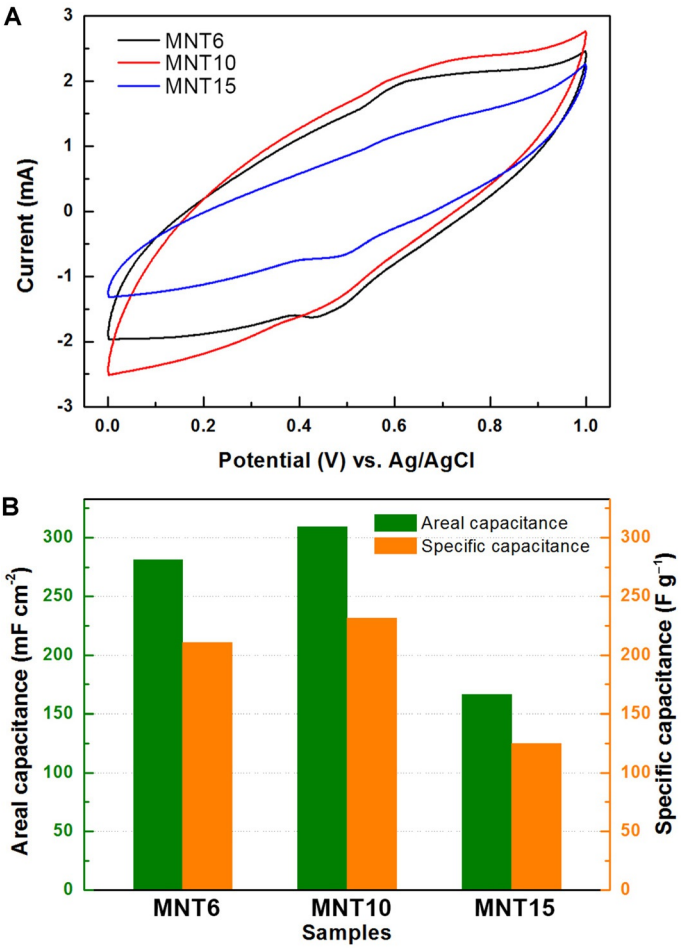

Figure 6. (A) CV curves of MNT6, MNT10, and MNT15 at the scan rate of 100 mV s^{-1}, and (B) capacitance comparison between them.

2 mA cm^{-2}. A possible reason for the deviation from standard symmetrical shapes for both the CV and charge/discharge curves is the relatively large internal resistance, which may be improved by constructing hybrids with other conductive matrices. The cycling stability of MNT10 was performed by CV cycling at a scan rate of 100 mV s^{-1} as shown in Figure 8D. After 2000 cycles, the specific capacitance of the MNT10 electrode still retains 98% of its initial value, suggesting remarkable cycling stability for the mesoporous MnO_2 nanotubes.

The electrochemical behavior of MNT-40, MNT-60, and MNT-90 was also evaluated for comparison. As shown in Figure 8A, MNT-60 exhibits the highest current intensity, implying the best electrochemical performance compared with those of MNT-40 and MNT-90. This is also confirmed by the galvanostatic charge/discharge curves (Figure 8B). Areal capacitances of 177, 303, and 180 mF cm^{-2} and specific capacitances of 137, 226, and 126 F g^{-1} are achieved for MNT-40, MNT-60, and MNT-60, respectively (Figure 8C). The Nyquist plots of MNT-40, MNT-60, and MNT-90 electrodes are displayed in Figure 8D, with the low-frequency region of MNT-60 being closest to the vertical line and demonstrating the best capacitive behavior. Compared with MNT-40 and MNT-90, the high-frequency loop is the smallest for MNT-60, indicating the lowest Faradaic charge transfer resistance, which is probably due to the fast and efficient ion/electrolyte transfer derived from loosely arranged subunits and larger intersheet spaces for MNT-60. In short, the best electrochemical performance of MNT-60 is derived from the mesoporous outer-shell and better electrical conductivity which is beneficial for electron transport and ion diffusion.

Conclusions

In summary, a novel method for the mass preparation of mesoporous MnO_2 nanotubes using electrospun CNFs as a sacrificial template has been demonstrated. The as-prepared dual-layer MnO_2 nanotubes are composed of an inner-shell of packed MnO_2, and an outer-shell of mesoporous sheet-like MnO_2. Parameters influencing the morphology of mesoporous MnO_2 nanotubes, including CNF fiber diameters and reaction temperatures, were investigated in detail. Results show that CNFs with moderate fiber diameters combined with a mild reaction temperature will lead to electrochemically more active MnO_2 nanotubes. Therefore, this study provides a new and versatile pathway for the preparation of MnO_2 nanotubes for potential applications in energy storage.

Experimental Section

Materials

Polyacrylonitrile (PAN, $M_w = 150\,000$ g mol^{-1}) was purchased from Sigma–Aldrich. Potassium permanganate ($KMnO_4$) and sodium sulfate (Na_2SO_4) were supplied by Sinopharm Chemical Reagent Co. Ltd. *N*,*N*-dimethylformamide (DMF) and ethanol were obtained from Shanghai Chemical Reagent Company. All aqueous solutions were prepared with doubly distilled water.

Preparation of MnO_2 nanotubes

The preparation procedure of mesoporous MnO_2 nanotubes (denoted as MNT) is schematically described in Scheme 1. Briefly, specific amount of PAN powder was first dissolved in 10 mL of DMF at room temperature under vigorous stirring overnight to form a homogeneous solution. For the electrospinning experiments, freshly prepared precursor solution was then transferred into a 5 mL plastic syringe and injected with a feeding rate of 0.2 mm min^{-1} through a No. 21 stainless steel needle connected to a high-voltage DC power supply. A rotating aluminum drum was grounded and set as the collector with a distance of 12 cm to the needle tip. When a fixed voltage of 20 kV was applied to the system, nanofibers were generated and deposited on the aluminum drum. After 30 min of electrospinning, a non-woven PAN membrane was formed and could be easily peeled off from the collector.

The pre-oxidation and carbonization treatments of the obtained PAN fiber membranes were performed in batches according to our previous report.[4] Typically, the dried PAN membranes were first pre-oxidized under an air atmosphere at 250 °C for 1 h with a heating rate of 1 °C min^{-1}. Then, samples were heated up to 900 °C at a rate of 5 °C min^{-1} and carbonized for 1 h under N_2 atmosphere. In order to produce CNFs with different fiber diameters, the PAN content in the precursor solution was varied by 6, 10, and 15 wt%, thus giving PAN and CNFs denoted as PAN6, PAN10, PAN15 and CNF6, CNF10, CNF15, respectively. Afterwards, 1 g of as-prepared self-standing CNF membranes were immersed into excess $KMnO_4$

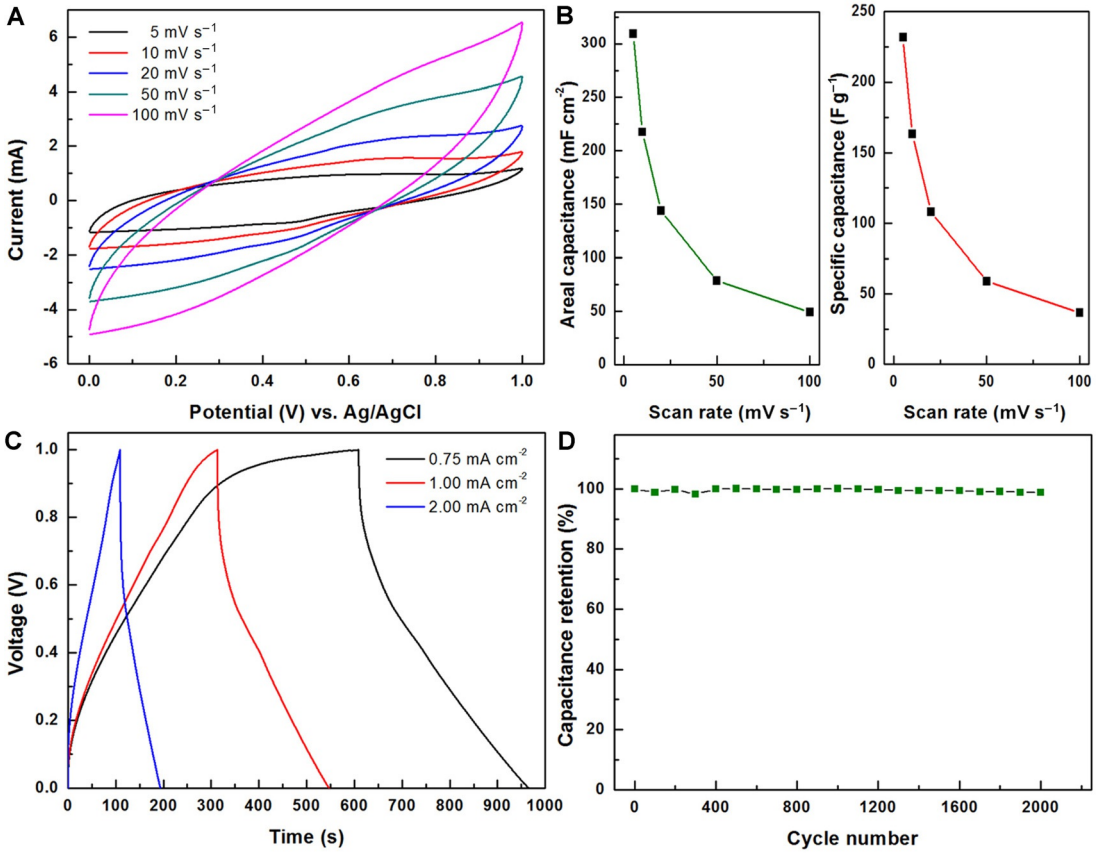

Figure 7. (A) CV curves of MNT10 at different scan rates (5, 10, 20, 50, 100 mV s^{-1}) in 0.5 M Na_2SO_4 aqueous solution. (B) Capacitance of MNT10 as a function of the scan rate. (C) Galvanostatic charge/discharge curves of MNT10 at different current densities. (D) Cycling stability test of MNT10 electrode measured in 0.5 M Na_2SO_4 aqueous solution at a scan rate of 100 mV s^{-1}.

aqueous solution and reacted at 70 °C in an oven according to the following well-known reaction shown in Equation (2):

$$3\,C + 4\,MnO_4^- + H_2O = 4\,MnO_2 + 2\,HCO_3^- + CO_3^{2-} \quad (2)$$

After 24 h of reaction, products were withdrawn and rinsed with DI water several times and absolute ethanol one time to remove the byproducts and vacuum dried before further measurements. The resulted products (MnO_2 nanotubes) are correspondingly denoted as MNT6, MNT10, and MNT15. Furthermore, MNT membranes were also prepared under different temperatures, that is, 40, 60, and 90 °C, using the same CNF10 membranes, and the corresponding MNTs thus obtained are denoted as MNT-40, MNT-60, and MNT-90, respectively.

Characterization

The morphology of the samples was investigated using field emission scanning electron microscope (FESEM, Zeiss) at an acceleration voltage of 5 kV. All samples were coated with a thin layer of gold prior to FESEM observations. Transmission electron microscopy (TEM) and high-resolution transmission electron microscopy (HRTEM) observations were performed under an acceleration voltage of 200 kV with a JEOL JEM 2100 TEM. X-ray diffraction (XRD) experiments were conducted from $2\theta = 10°$ to 80° on an X'Pert Pro X-ray diffractometer with $Cu_{K\alpha}$ radiation ($\lambda = 0.1542$ nm) under a voltage of 40 kV and a current of 40 mA. X-ray photoelectron spectroscopy (XPS) analyses were made with a VG ESCALAB 220I-XL device. All XPS spectra were corrected using C 1s line at 284.6 eV.

Electrochemical measurements

The electrochemical properties of the as-prepared electrode materials were performed using a CHI 660D electrochemical workstation (Shanghai Chenhua Instrument Co., China) in a standard three-electrode setup, where a platinum wire was used as the counter electrode and a Ag/AgCl electrode was used as the reference electrode. The working electrode was prepared by pressing a piece of precut MnO_2 nanotube membrane between two nickel foam pieces. Cyclic voltammetry (CV) curves collected at different scan rates and galvanostatic charge/discharge curves were obtained in a potential range from 0 to 1.0 V. AC impedance measurements were carried out from 10^{-2} to 10^6 Hz with an AC amplitude of 5 mV. All the tests were performed in a N_2 saturated 0.5 M Na_2SO_4 solution.

Acknowledgements

The authors are grateful for the financial support from the National Natural Science Foundation of China (51433001, 51373037, 51125011).

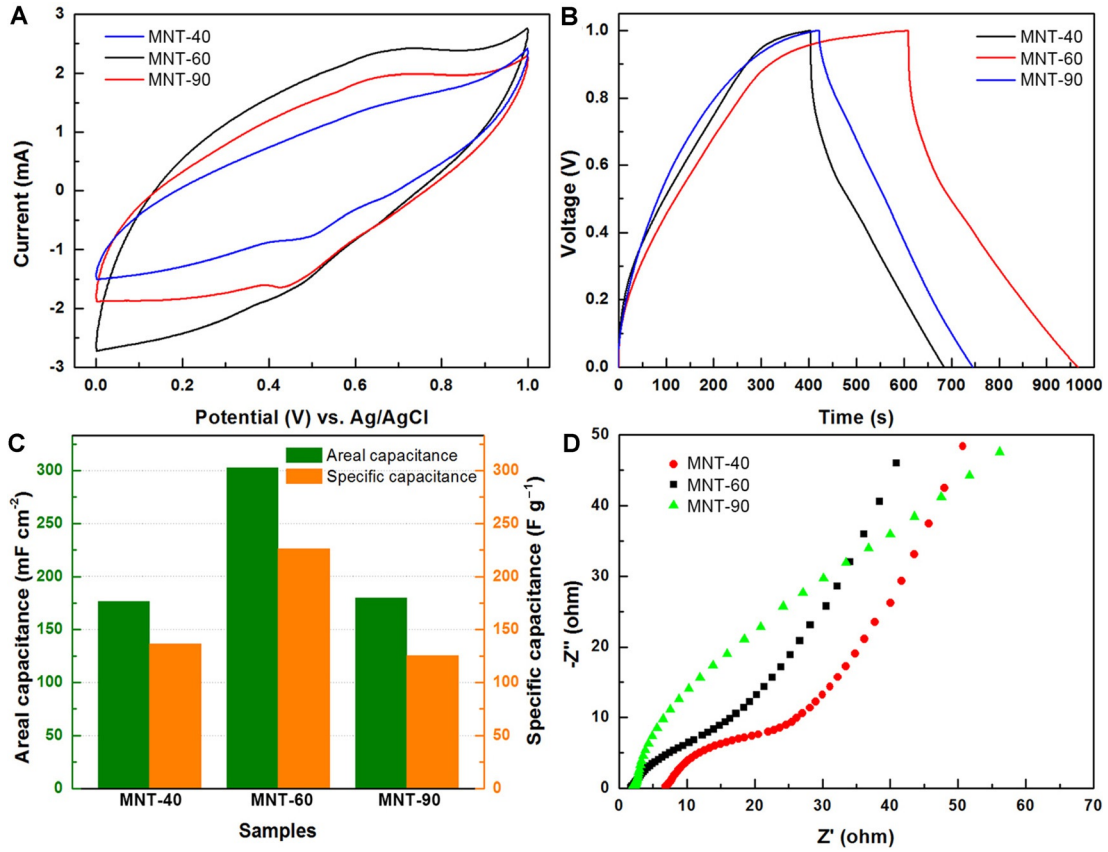

Figure 8. (A) CV curves of MNT-40, MNT-60, and MNT-90 at a scan rate of 100 mV s^{-1}. (B) Galvanostatic charge/discharge curves of different MNTs at a current density of 0.75 mA cm^{-2}. (C) Capacitance comparison between MNT-40, MNT-60, and MNT-90. (D) Impedance Nyquist plots of MNT-40, MNT-60, and MNT-90.

Keywords: carbon · electrospinning · MnO_2 nanotubes · nanofibers · supercapacitors

[1] S. S. Lee, H. W. Bai, Z. Y. Liu, D. D. Sun, *Appl. Catal. B* **2013**, *140–141*, 68–81.
[2] X. Wang, H. Q. Fan, P. R. Ren, *Catal. Commun.* **2013**, *31*, 37–41.
[3] Z. L. Wang, D. Xu, J. J. Xu, X. B. Zhang, *Chem. Soc. Rev.* **2014**, *43*, 7746–7786.
[4] Y. P. Huang, Y. E. Miao, S. S. Ji, W. W. Tjiu, T. X. Liu, *ACS Appl. Mater. Interfaces* **2014**, *6*, 12449–12456.
[5] T. Maiyalagan, J. Sundaramurthy, P. S. Kumar, P. Kannan, M. Opallo, S. Ramakrishna, *Analyst* **2013**, *138*, 1779–1786.
[6] C. Peng, G. G. Li, D. L. Geng, M. M. Shang, Z. Y. Hou, J. Lin, *Mater. Res. Bull.* **2012**, *47*, 3592–3599.
[7] A. Ghosh, E. J. Ra, M. H. Jin, H. Jeong, T. H. Kim, C. Biswas, Y. H. Lee, *Adv. Funct. Mater.* **2011**, *21*, 2541–2547.
[8] J. Yan, E. Khoo, A. Sumboja, P. S. Lee, *ACS Nano* **2010**, *4*, 4247–4255.
[9] X. L. Huang, J. Chai, T. Jiang, Y. J. Wei, G. Chen, W. Q. Liu, D. X. Han, L. Niu, L. M. Wang, X. B. Zhang, *J. Mater. Chem.* **2012**, *22*, 3404–3410.
[10] Z. Wu, X. L. Huang, Z. L. Wang, J. J. Xu, H. G. Wang, X. B. Zhang, *Sci. Rep.* **2014**, *4*, 3669.
[11] G. M. Wang, H. Y. Wang, Y. C. Ling, Y. C. Tang, X. Y. Yang, R. C. Fitzmorris, C. Wang, J. Z. Zhang, Y. Li, *Nano Lett.* **2011**, *11*, 3026–3033.
[12] L. L. Zhang, X. B. Zhang, Z. L. Wang, J. J. Xu, D. Xu, L. M. Wang, *Chem. Commun.* **2012**, *48*, 7598–7600.
[13] H. Y. Chen, T. L. Zhang, J. Fan, D. B. Kuang, C. Y. Su, *ACS Appl. Mater. Interfaces* **2013**, *5*, 9205–9211.
[14] G. R. Yang, W. Yan, J. N. Wang, H. H. Yang, *CrystEngComm* **2014**, *16*, 6907–6913.
[15] H. Xia, J. K. Feng, H. L. Wang, M. O. Lai, L. Lu, *J. Power Sources* **2010**, *195*, 4410–4413.
[16] Y. E. Miao, R. Y. Wang, D. Chen, Z. Y. Liu, T. X. Liu, *ACS Appl. Mater. Interfaces* **2012**, *4*, 5353–5359.
[17] Y. E. Miao, S. X. He, Y. L. Zhong, Z. Yang, W. W. Tjiu, T. X. Liu, *Electrochim. Acta* **2013**, *99*, 117–123.
[18] M. Y. Wang, J. Ioccozia, L. Sun, C. J. Lin, Z. Q. Lin, *Energy Environ. Sci.* **2014**, *7*, 2182–2202.
[19] J. G. Yu, G. P. Dai, B. B. Huang, *J. Phys. Chem. C* **2009**, *113*, 16394–16401.
[20] E. Eustache, P. Tilmant, L. Morgenroth, P. Roussel, G. Patriarche, D. Troadec, N. Rolland, T. Brousse, C. Lethien, *Adv. Energy Mater.* **2014**, *4*, 13016128.
[21] C. Tang, Q. Zhang, M. Q. Zhao, G. L. Tian, F. Wei, *Nano Energy* **2014**, *7*, 161–169.
[22] L. Li, Z. Wu, S. Yuan, X. B. Zhang, *Energy Environ. Sci.* **2014**, *7*, 2101–2122.
[23] Z. Y. Zhang, F. Xiao, L. H. Qian, J. W. Xiao, S. Wang, Y. Q. Liu, *Adv. Energy Mater.* **2014**, *4*, 1400064.
[24] J. Zhu, Z. Xu, B. N. Lu, *Nano Energy* **2014**, *7*, 114–123.
[25] Z. J. Fan, J. Yan, L. J. Zhi, Q. Zhang, T. Wei, J. Feng, M. L. Zhang, W. Z. Qian, F. Wei, *Adv. Mater.* **2010**, *22*, 3723–3728.
[26] M. Kaempgen, C. K. Chan, J. Ma, Y. Cui, G. Gruner, *Nano Lett.* **2009**, *9*, 1872–1876.
[27] M. Remskar, A. Mrzel, Z. Skraba, A. Jesih, M. Ceh, J. Demšar, P. Stadelmann, F. Lévy, D. Mihailovic, *Science* **2001**, *292*, 479–481.
[28] W. Xiao, H. Xia, J. Y. H. Fuh, L. Lu, *J. Power Sources* **2009**, *193*, 935–938.
[29] D. D. Han, X. Y. Jing, P. C. Xu, Y. S. Ding, J. Y. Liu, *J. Solid State Chem.* **2014**, *218*, 178–183.
[30] Y. P. Huang, Y. E. Miao, W. W. Tjiu, T. X. Liu, *RSC Adv.* **2015**, *5*, 18952–18959.
[31] Y. F. Shen, R. P. Zerger, R. N. DeGuzman, S. L. Suib, L. McCurdy, D. I. Potter, C. L. O'Young, *Science* **1993**, *260*, 511–515.
[32] Y. S. Ding, X. F. Shen, S. Sithambaram, S. Gomez, R. Kumar, V. M. B. Crisostomo, S. L. Suib, M. Aindow, *Chem. Mater.* **2005**, *17*, 5382–5389.

[33] J. Y. Tao, N. S. Liu, W. Z. Ma, L. W. Ding, L. Y. Li, J. Su, Y. H. Gao, *Sci. Rep.* **2013**, *3*, 2286.
[34] J. P. Liu, J. Jiang, C. W. Cheng, H. X. Li, J. X. Zhang, H. Gong, H. J. Fan, *Adv. Mater.* **2011**, *23*, 2076 – 2081.
[35] J. F. Wang, G. Zhu, L. J. Deng, L. P. Kang, Z. P. Hao, Z. H. Liu, *CrystEngComm* **2012**, *14*, 8253 – 8260.
[36] W. B. Yan, T. Ayvazian, J. Y. Kim, Y. Liu, K. C. Donavan, W. D. Xing, Y. G. Yang, J. C. Hemminger, R. M. Penner, *ACS Nano* **2011**, *5*, 8275 – 8287.
[37] L. Y. Yuan, X. H. Lu, X. Xiao, T. Zhai, J. J. Dai, F. C. Zhang, B. Hu, X. Wang, L. Gong, J. Chen, C. G. Hu, Y. X. Tong, J. Zhou, Z. L. Wang, *ACS Nano* **2012**, *6*, 656 – 661.
[38] X. Zhang, X. Z. Sun, H. T. Zhang, C. Li, Y. W. Ma, *Electrochim. Acta* **2014**, *132*, 315 – 322.
[39] P. Yu, X. Zhang, D. L. Wang, L. Wang, Y. W. Ma, *Cryst. Growth Des.* **2009**, *9*, 528 – 533.
[40] Y. Dzenis, *Science* **2004**, *304*, 1917 – 1919.
[41] A. Greiner, J. H. Wendorff, *Angew. Chem. Int. Ed.* **2007**, *46*, 5670 – 5703; *Angew. Chem.* **2007**, *119*, 5770 – 5805.
[42] M. Inagaki, Y. Yang, F. Kang, *Adv. Mater.* **2012**, *24*, 2547 – 2566.
[43] Y. P. Huang, Y. E. Miao, L. S. Zhang, W. W. Tjiu, J. S. Pan, T. X. Liu, *Nanoscale* **2014**, *6*, 10673 – 10679.
[44] H. O. Pierson, *Handbook of Carbon, Graphite, Diamond, and Fullerenes: Properties, Processing, and Applications*, Noyes Publications, **1993**.
[45] W. Xiao, D. L. Wang, X. W. Lou, *J. Phys. Chem. C* **2010**, *114*, 1694 – 1700.

Manuscript received: January 29, 2015
Final article published: May 13, 2015